Self-diffusion of spherocylindrical particles flowing under non-uniform shear rate†

D. Hernández-Delfin, [ID] *[ab] T. Weinhart [ID] [c] and R. C. Hidalgo*[a]

This work is devoted to study numerically the self-diffusion of spherocylindrical particles flowing down an inclined plane, using the discrete element method (DEM). This system is challenging due to particles being non-spherical and because they are subjected to a non-uniform shear rate. We performed simulations for several aspect ratios and inclination angles, tracking individual particle trajectories. Using the simulation data, we computed the diffusion coefficients D, and a coarse-graining methodology allowed accessing the shear rate spatial profiles $\dot{\gamma}(z)$. This data enabled us to identify the spatial regions where the diffusivity strongly correlates with the local shear rate. Introducing an effective particle size $d_\perp$, we proposed a well-rationalized scaling law between D and $\dot{\gamma}$. Our findings also identified specific locations where the diffusivity does not correlate with the shear rate. This observation corresponds to zones where $\dot{\gamma}$ has non-linear spatial variation, and the velocity probability density distributions exhibit asymmetric shapes.

1 Introduction

Granular flows commonly appear in natural and technological processes, and their rheology depends on a multitude of factors, such as the grains' shape, hardness, and friction. Here, we study the self-diffusion of the grains, which results from the random fluctuations of their motion, induced by the unceasing inelastic collisions. Diffusion even occurs when granular flows are in steady-state conditions, and it shows analogous behavior to the thermal diffusion of molecules in dense gases,[1,2] even though granular materials are athermal. Hence, diffusion theory is a pillar of granular hydrodynamic models, describing the macroscopic response of granular systems.

Self-diffusion in dilute and dense ensembles of macroscopic disks and spheres has been studied experimentally[3,4] and theoretically.[5–14] All these investigations focused on addressing scaling laws[15] that relate the self-diffusion transport coefficient D to the particle diameter d, the shear rate $\dot{\gamma}$, the granular temperature T, or the effective inertial number $I = \mathrm{d}\dot{\gamma}/\sqrt{P/\rho}$,

with P and ρ indicating the pressure and particle density, respectively.

To model how diffusion occurs, we need to account for the macroscopic density of the granular system: in dilute systems, the analysis is typically done assuming the collisions are binary, which is very plausible. However, this assumption fails in dense scenarios. Three main scaling laws predicting particle diffusivity have been observed: in dilute systems, theoretical and numerical approaches have proven that $D \sim d\sqrt{T}$.[5,14,16] In dense situations, simulations of quasi-static flows for low inertial numbers $I \lesssim 0.01$ resulted in $D \sim d^2\dot{\gamma}/\sqrt{I}$.[12,13] In rapid dense granular flows, experiments[3,4] and simulations[11–14] have suggested the diffusivity scales as $D \sim d^2\dot{\gamma}$.

In the past, several authors have numerically explored the self-diffusivity of particles within uniform shear-rate conditions, which is generally attained by applying Lees–Edwards' boundary conditions in the absence of gravity.[6,14,17,18] The advantage of this method is that it allows deducing the value of D as an average over the whole spatial domain. Nevertheless, systems under non-uniform shear rate $\dot{\gamma}$ are more frequent in nature and industrial processes. Thus, researchers have paid efforts in investigating self-diffusion of particles in rapid granular flows such as: rotating drums,[4] inclines,[19] and heaps.[11,19,20] For open and closed heaps, Y. Fan et al. made the remarkable observation that particle size and shear rate determine self-diffusion at relatively high shear rates. At low shear rates, however, self-diffusion is a phenomenon totally governed by the particle stiffness and the intensity of the external field.[11]

Researchers have also found that the scaling law $D \sim d^2\dot{\gamma}$ for dense rapid flows is still valid for mixtures of particles that

[a] Departamento de Física y Matemática Aplicada, Universidad de Navarra, P.O. Box. 177, E-31080 Pamplona, Spain. E-mail: dhernandezd@alumni.unav.es, raulcruz@unav.es

[b] BCAM - Basque Center for Applied Mathematics, Mazarredo, 14 E48009 Bilbao, Basque Country Spain

[c] Multiscale Mechanics, Department of Thermal and Fluid Engineering, Faculty of Engineering Technology, MESA+, University of Twente, P.O. Box. 217, 7500 AE Enschede, The Netherlands

† Electronic supplementary information (ESI) available. See DOI: https://doi.org/10.1039/d1sm01436f

differ in size[21,22] or density.[19] However, the case of non-spherical particles has been less studied, though they are ubiquitous in nature and industry. Investigating the phenomenon of self-diffusion in polydisperse non-spherical ensembles is challenging, due to the need to differentiate self-diffusion from other complex mechanisms involved in macroscopic mixing and segregation. In fact, monodisperse assemblies of non-spherical particles are suitable to isolate diffusion from other mechanisms. Recently, R. Cai et al.[23] numerically examined self-diffusion in a system of ellipsoids, using Lees-Edwards boundary conditions, and varying the particle aspect ratio systematically. They proposed a generalized scaling law for the diffusivity in the direction perpendicular to the flow in terms of an effective particle size d_{eff}, the aspect ratio ξ and the solid fraction ϕ, namely, $D \sim \chi (\phi, \xi) \dot{\gamma} d_{eff}^2$. It is worth mentioning that H. Ma and Y. Zhao investigated the flow of ellipsoidal particles in a horizontal rotating drum[24] in the rolling regime, i.e., particles moving under non-uniform shear rate. They detected differences in the slopes of mean squared displacements curves (MSD) for particles with different shapes under the same excitation conditions. However, they neither computed the self-diffusion coefficient nor evaluated its dependence on the shear rate.

Here, we numerically investigate the self-diffusion in a dense rapid flow of sphero-cylindrical particles driven by gravity down an inclined plane. This system is challenging not only because particles are non-spherical, but also because they are submitted to a non-uniform shear rate. In addition, there are places where the shear rate profile varies nonlinearly along the direction perpendicular to the incline. The work is organized as follows: in Section 2, the numerical algorithm is summarized and the model system is described. In Section 3, the numerical results are presented, and the scaling analysis is elaborated and discussed. Finally, conclusions are given, and ideas for improvement and further work are proposed.

2 Numerical method

2.1 DEM simulations details

For simulations, the discrete element method (DEM) is adopted. Specifically, we employ a 3D, hybrid CPU-GPU implementation introduced earlier.[25,26] The modeled particles are shapes composed of a cylinder of length l and diameter d, and two hemispherical ends of diameter d. Thus, the particle's aspect ratio can be defined as $\xi = L/d$, where $L = (l + d)$ is the particle total length.

The DEM framework resolves the translational and rotational equations of motion of each particle i ($i = 1,\ldots, N_p$). It considers body forces like gravity as well as pairwise interactions between contacting particles i and j. The contact force $\mathbf{F}_{ij}$ includes a tangential and normal component, $\mathbf{F}_{ij} = \mathbf{F}_{ij}^n + \mathbf{F}_{ij}^t$. The normal force reads $\mathbf{F}_{ij}^n = - k^n \delta^n - \gamma^n v_{rel}^n$, where k^n is the spring constant in the normal direction, δ_n denotes the overlap between particles, γ^n is the normal damping coefficient and v_{rel}^n is the normal relative velocity between particles i and j.

The tangential force $\mathbf{F}_{ij}^t$ also contains an elastic term and a frictional term, accounting for friction between the grains. Taking into account Coulomb's friction constraint, which reads $F^t = \min\{-k^t\delta^t - \gamma^t|v_{rel}^t|, \mu F^n\}$, where μ is the friction coefficient, γ^t is the damping coefficient in tangential direction, v_{rel}^t is the tangential component of the relative contact velocity of the overlapping pair. δ^t represents the elastic deformation of an imaginary spring with spring constant k^t at the contact, which increases as $d\boldsymbol{\delta}(t)/dt = \mathbf{v}_{rel}^t$ as long as there is an overlap between the interacting particles. The elastic tangential elongation $\boldsymbol{\delta}^t$ is kept orthogonal to the normal vector (truncated if necessary).[27]

The equations of motion read as

$$\sum_{\substack{j=1\\j\neq i}}^{N_c} \mathbf{F}_{ij} + m_i\mathbf{g} = m_i\dot{\mathbf{v}}_i \tag{1a}$$

$$\sum_{\substack{j=1\\j\neq i}}^{N_c} \boldsymbol{\tau}_{ij} = \mathscr{I}_i\dot{\boldsymbol{\omega}}_i + \boldsymbol{\omega}_i \times (\mathscr{I}_i\boldsymbol{\omega}_i) \tag{1b}$$

where m_i and $\mathscr{I}_i$ are the mass and the moment of inertia tensor of the particle i, respectively, and N_c accounts for the number of contacts for each particle i. $\boldsymbol{\tau}_{ij}$ are the torques corresponding to each contacting force $\mathbf{F}_{ij}$, since they generally are non-central forces. $\mathbf{g}$ represents the acting gravitational acceleration. Moreover, $\mathbf{v}_i$ and $\boldsymbol{\omega}_i$ are the translational and rotational velocities whose integrations are performed differently. A velocity Verlet numerical algorithm[28] is used to integrate the translational equations of motion of each particle, while the rotational degrees of freedom were resolved using a modified leap-frog algorithm.[29]

2.2 Chute flow of sphero-cylindrical particles

Recently, the macroscopic properties of a chute flow of sphero-cylindrical particles driven by gravity were investigated.[26] Here we adopt the same configuration but focusing on the random motion of each particle. We perform a systematic study, exploring the impact of the particle shape on the individual particle motion. For the sake of simplicity, the length of the particle is fixed at $L = 2/16m$, and several aspect ratios $\xi = \{1.00, 1.01, 1.30, 1.50, 2.00, 2.50, 3.00\}$ are studied.

The simulation domain is a 3D rectangular box. In the directions x and y, the system dimensions are fixed to $\Delta X = \Delta Y = 16 \times L$ and periodic boundaries conditions are used. Thus, once a particle reaches the extremes of the domain along the x and y axis, it re-enters the domain on the opposite side with the same velocity and orientation. This, combined with the fact that the particles located in regions close to one extreme can interact with particles in the another one, ensures the periodicity of the system. In direction z, the bulk thickness $\Delta Z(\xi)$ is kept constant to about $20L$ by varying the number of particles. We consider that the gravitational field acts in the x–z plane, forming an angle α with the x-axis. Thus, gravity acts in direction $\mathbf{g} = g [\sin \alpha, 0, -\cos \alpha]$ with magnitude $g = 1$ m s^{-2}. To avoid extreme crystallization of the flow, a bottom plate is built of spherical particles with radius $R = L/2$, placed randomly.

This procedure reproduces the macro and microscopic conditions presented in ref. 30 (see it for more details).

Granular flows down inclined surfaces are typically characterized by two critical angles. For angles below α_{c1}, friction dominates over gravity, and the system is at rest. However, above an inclination α_{c2}, gravity dominates over friction, and the material accelerates. Between these two angles, steady flow is possible. In ref. 26, the values of $\alpha_{c1}(\xi)$ and $\alpha_{c2}(\xi)$ corresponding to granular beds of $\Delta Z \approx 20 \times L$ were identified accurately. Here, we focus on the steady-flow configurations, examining inclinations in the regime $\alpha_{c1}(\xi) < \alpha < \alpha_{c2}(\xi)$ for each elongation ξ, which guaranties steady-state conditions in all cases (see ref. 26).

In the calculations the particle density was $\rho_p = 2600$ kg m^{-3}, and the stiffness was set to $k^n = 2 \times 10^5$ $(m_p g/l)$ and $k^t = 2/7k^n$, where m_p is the particle mass. The particle friction was $\mu = 0.5$ and the dissipation coefficients γ^n, γ^t were set by setting effective restitution coefficients e_n, $\beta = \dfrac{\ln e_n}{\sqrt{\ln e_n^2 + \pi^2}}$ in normal and tangential direction, respectively. A simulation time step was chosen equal to $\delta t = t_c/50$, where t_c is the contact time.

The DEM algorithm is able to model the trajectories of all particles, during the simulation. Fig. 1(a) illustrates the trajectories of twenty randomly chosen particles after reaching the steady regime. The data correspond to the case $\xi = 2.5$ and $\alpha = 31.0°$.

2.3 Coarse-graining average

A useful approach to obtain macroscopic fields is the called coarse-graining technique. With this technique, density $\rho(\mathbf{r}, t)$, velocity $\mathbf{V}(\mathbf{r}, t)$, and the kinetic part of the stress tensor $\boldsymbol{\sigma}^k(\mathbf{r}, t)$ fields are obtained from individual positions $\mathbf{r}_i$ and velocities $\mathbf{v}_i$ using the methodology described in ref. 30–33. The methodology requires a non-negative integrable function that maps the microscopic details into macroscopic fields.

Here, we use a truncated Gaussian function $\phi_i(\mathbf{r}) = A_\omega^{-1} \exp[-(\mathbf{r} - \mathbf{r}_i)^2/2\omega^2]$, the cutoff distance is $r_c = 4\omega$ and

Fig. 1 (a) Trajectories of twenty randomly chosen particles after reaching the steady regime. (b) Snapshot of the numerical setup; the red curve indicates the mean value of the x-component of the velocity profile along the z-direction, $\bar{v}_x(z)$. The figures correspond to the case $\xi = 2.5$ and $\alpha = 31.0°$. A particle's color quantifies the x-component of its velocity. Note that gravity $\mathbf{g}$ acts at an angle α to the vertical direction.

$\omega = L/4$. The contact stress $\boldsymbol{\sigma}^c(\mathbf{r}, t)$ field is computed from forces and branch vectors $\mathbf{r}_{ij}$ using the function ψ_{ij}, which is the lineal integral $\mathbf{r}_{ij}$, $\psi_{ij} = \int_0^1 \psi(\mathbf{r} - \mathbf{r}_i + s\mathbf{r}_{ij})\mathrm{d}s$, thus $\boldsymbol{\sigma}_{ij}^c(\mathbf{r}, t) = \mathbf{r}_{ij} \otimes \mathbf{F}_{ij}\psi_{ij}$. The total stress results in $\boldsymbol{\sigma}(\mathbf{r}, t) = \boldsymbol{\sigma}^k(\mathbf{r}, t) + \boldsymbol{\sigma}^c(\mathbf{r}, t)$.

For the sake of simplicity, our analysis is done in steady-state conditions. The steady-state momentum balance requires that the stress divergence and gravitational forces are in balance[27],

$$\sigma_{xz}/\sigma_{zz} = \tan \alpha. \qquad (2)$$

The simulations are executed until the system's kinetic energy reaches a constant value, approximately after 160 seconds. Thus, using the averaged fields σ_{xz} and σ_{zz}, the validity of eqn (2) is proven (see ref. 26), and will be used to determine when the system is in steady state.

Once the system is in steady-state, the macroscopic fields are averaged over 240 seconds, sampling every 1.0 seconds. As the results are practically uniform in the x- and y-directions, we further averaged over those directions. Thus, we obtained the time-, width-, and length-averaged density $\rho(z)$, linear momentum density $P_x(z)$, and velocity $V_x(z) = P_x(z)/\rho(z)$. As a result, the local shear rate field $\dot{\gamma}(z) = \dfrac{\mathrm{d}V_x(z)}{\mathrm{d}z}$ is accessed. The spatial profiles of the coarse-grained contact stress, $\sigma_{\alpha\beta}^c(\mathbf{r})$, were also computed in all cases. Our outcomes are totally consistent with earlier findings.[26] Fig. 1(b) illustrates both the numerical set-up and the velocity field corresponding to the case $\xi = 2.5$ and $\alpha = 31.0°$. The red curve indicates the x-component of the velocity profile along the z-direction, $\bar{v}_x(z)$. The color map also quantifies the $v_x(z)$ values. Note that gravity g forms an angle α with the vertical direction.
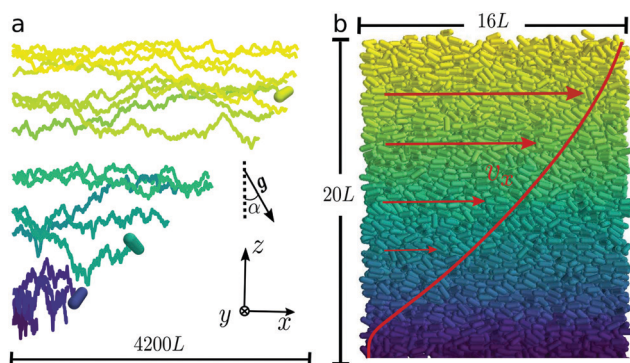
3 Results

Although the particles experience a complex 3D motion, our analysis is focused on the diffusivity along the z-direction only. The results are therefore related to the diffusion in the direction perpendicular to the advective plane. Firstly, we examine the particles' mean squared displacements (MSD) as a function of the time-lag τ. MSD is calculated as
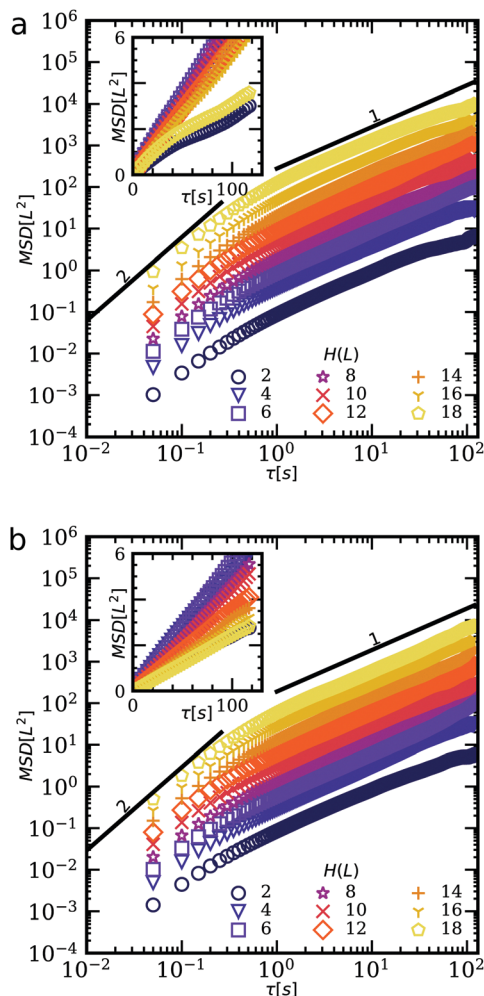
$$\mathrm{MSD}(\tau) = \frac{1}{N_k} \sum_i^{N_k} (z_i(\tau + t) - z_i(t))^2$$

averaged over specific particle ensembles with N_k particles, with a mean trajectory located at the same vertical position. As the shear rate $\dot{\gamma}(z)$ is variable, we split the system in vertical direction into 20 blocks of width $\Delta H = L$ in terms of the particle's longest side L. Thus, the particles whose mean trajectory are located in each block are roughly submitted to the same $\dot{\gamma}$.

Fig. 2 shows examples of the MSD(τ) curves (in log–log scale) for a subset of the sections labeled with H representing the region height $z = H$. The insets illustrate the same data but using linear scale. The outcomes correspond to two systems, in (a) aspect ratio $\xi = 1.3$ and inclination $\alpha = 27°$ and (b) aspect

Fig. 2 The mean squared displacements (MSD) *vs.* τ for the cases (a) ξ = 1.3, α = 27° and (b) ξ = 2.5, α = 30° (both in log–log scales). Each curve represents the MSD calculated for each block of base equivalent to the system and width L whereas lines show the powers 1 and 2. In both cases, the inset shows the same but on linear scale.
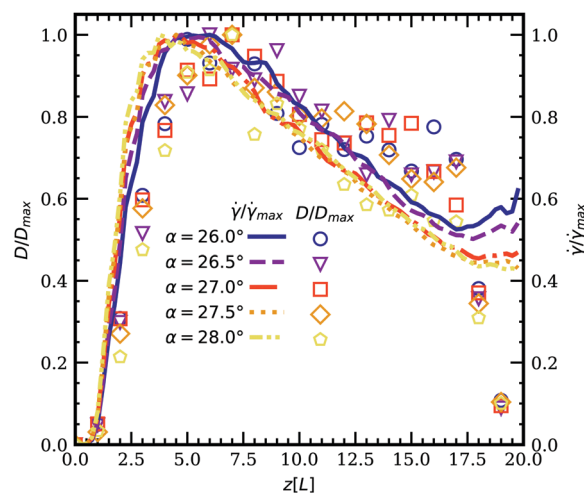
the slope seems to vary non-monotonically with the height, which is expected as $\dot{\gamma}(z)$ also varies in that way.

Going deeper inside the previous observations, we determine the diffusion coefficient D and the shear rate $\dot{\gamma}$ corresponding to each region. Fig. 3 and 4 display the profiles of $D(z)$ and normalized by the maximum diffusion coefficient D_{max} and the maximum shear rate $\dot{\gamma}_{max}$ for ξ = 1.3 and ξ = 2.5, respectively. Remarkably, the spatial profiles indicate that the local values of D and $\dot{\gamma}$ strongly correlate in practically the whole system, regardless of the value of $\dot{\gamma}_{max}$. However, for $z \lesssim 5L$, the values which correspond with $\dot{\gamma} < \dot{\gamma}_{max}$, tend to separate in both cases. Moreover, for smaller ξ, the profiles also tend to decorrelate as z increases. A similar split into three distinct regions was observed in ref. 34, which analysed the flow profiles of chute flows composed of monodisperse spherical particles. The central region, where D and $\dot{\gamma}$ strongly correlate, corresponds to the region where the local $\mu(I)$-rheology holds. That is, flowing conditions where the local $\dot{\gamma}(z)$ is only determined by the local shear stress $\sigma(z)$, and the flow resistance is only function of the local $\dot{\gamma}(z)$. However, the flow between the basal surface and the peak in shear rate showed boundary-layer effects; and the top layer showed effects of dilation due to the vanishing pressure. Indeed, the same effects likely affect the $D(\dot{\gamma})$-relation.

To assess the last argument, we plot the probability density function (PDF) of the vertical velocity $v_z(z, t)$ for the different blocks in Fig. 5(a) and (b). PDFs have been standardized to compare with the Gaussian distribution. In general, the outcome evidence a good agreement with a Gaussian shape, detecting small discrepancies at the tails. Furthermore, the statistics corresponding to the blocks closer to the bottom or the surface of the bed posses shapes, which differ from the Gaussian shape, noticeably. Additionally, Fig. 5 shows the third moments, also known as skewness, of the PDFs as a function of z, whereby the asymmetry is characterized. The results show that the PDFs tend to be more asymmetric for the heights

ratio ξ = 2.5 and inclination α = 30°. The resolution of τ is δ_τ = 0.05 s and the particles are followed during a total time elapsed of τ_T = 120 s = 12 000δ_τ. As a reference, the graphs include continuous lines representing power-law functions with exponent 2 and 1, indicating the ballistic and diffusive limit, respectively. As noticed, in all cases, the MSD curves seem to change their behavior close to $\tau \approx 1$ s. In detail, for $\tau < 1$ s, the movement of the particles is ballistic, while the movement is diffusive for $\tau > 1$ s. Note that the limited range of the explored $\dot{\gamma}$ values leads to the same transition time-lag $\tau \approx 1$ s, approximately.

Assuming, $\langle z(\tau)^2 \rangle = 2D\tau$, the diffusion coefficient can thus be computed from the slope of each curve in the region $\tau > 1$ s. In the insets of Fig. 2(a) and (b), it is noticeable that the slopes of the curves vary. For the sake of clarity, in the main figures, the data values have been distinctly shifted in the *y*-direction, highlighting the two different motion regimens. Interestingly,

Fig. 3 Plots of D/D_{max} (markers) and $\dot{\gamma}/\dot{\gamma}_{max}$ (curves) against the height z for ξ = 1.3 and several inclinations. The sets $\dot{\gamma}_{max}$ = [0.013, 0.017, 0.022, 0.026, 0.031] s^{-1} and D_{max} = [0.026, 0.034, 0.038, 0.042, 0.056] L^2 s^{-1} correspond to α = [26.0, 26.5, 27.0, 27.5, 28.0]°.

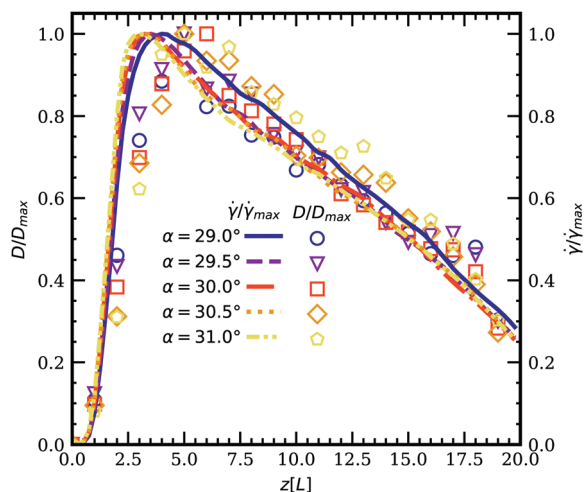**Fig. 4** Plots of D/D_{max} and $\dot\gamma/\dot\gamma_{max}$ against the height z for $\xi = 2.5$ and several inclinations. The sets $\dot\gamma_{max} = [0.022, 0.034, 0.045, 0.058, 0.071]$ s^{-1} and $D_{max} = [0.016, 0.022, 0.029, 0.036, 0.042]$ L^2 s^{-1} correspond to $\alpha = [29.0, 29.5, 29.0, 29.5, 30.0]°$.
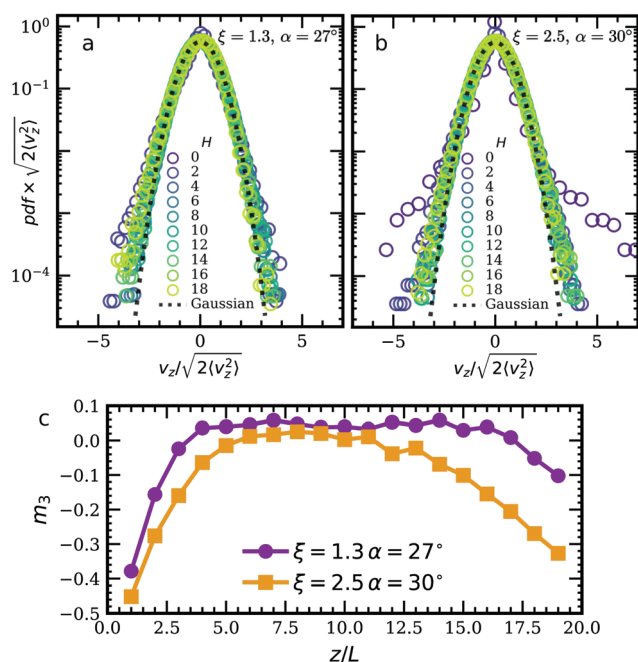

Fig. 5 Vertical velocity v_z PDFs standardized for comparison for (a) $\xi = 1.3$, $\alpha = 27°$ and (b) $\xi = 2.5$, $\alpha = 30°$. (c) Displays the skewness of PDFs against z.

where D and $\dot\gamma$ profiles deviate from each other, consistent with the particles in these zones follow a diffusive regime affected by variations in $\dot\gamma$.

To determine the scaling relation between D and $\dot\gamma$, it is necessary to identify the most relevant particle length scale, of interest for diffusion on the direction perpendicular to the macroscopic flow. In ref. 26, the particle size perpendicular to the flow direction, $d_\perp(\xi)$, was found to be an appropriate length scale to define an effective inertial number, I_{eff}. Note that this
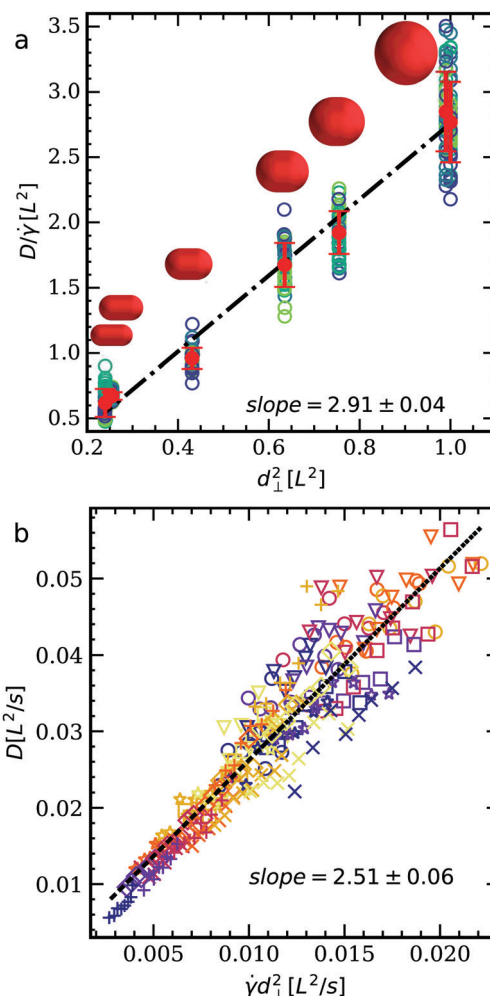

Fig. 6 (a) Ratio of diffusion coefficient and shear rate, $D/\dot\gamma$, plotted against the square of the characteristic particle length $d_\perp^2$ for all inclinations α and elongations ξ. The red points are the mean values of all $D/\dot\gamma$ for each ξ, and the error bars indicate the standard deviation thereof. The black line represents the resultant linear fit. For all ξ values, a representation of the particle is illustrated. (b) Measured D values against $\cdot$ $\dot\gamma d_\perp^2$. The result of the linear regression is represented by the line, and the obtained slope is annotated. For both plots, only D, γ values from the central part of the flow ($6L < z < 14L$) are shown.

length scale only depends on ξ ($d_\perp(\xi)$) and neither on the inclination angle α nor the height z, as was evidenced in the same work.[26] In detail, $d_\perp$ is obtained by finding the mean area of the orthographic projection of the particles, and then, the diameter of the area-equivalent circle is employed. For spherocylinders, $d_\perp^2 = 4/\pi(dl\langle\cos(\theta)\rangle + \pi d^2/4)$, where $l\langle\cos(\theta)\rangle$ is the averaged projection of the particles with respect to the vertical direction.

Motivated by this outcome, Fig. 6(a) displays $D/\dot\gamma$ as a function $d_\perp^2$. As a characteristic length scale $d_\perp$, we use the diameter of the orthographic projection of the particle on the plane perpendicular to the flow lines. In all cases, the data displayed corresponds to the range $6L < z < 14L$, avoiding the values close to the bottom plane neither the free surface. The data is rationalized using the mean value and standard
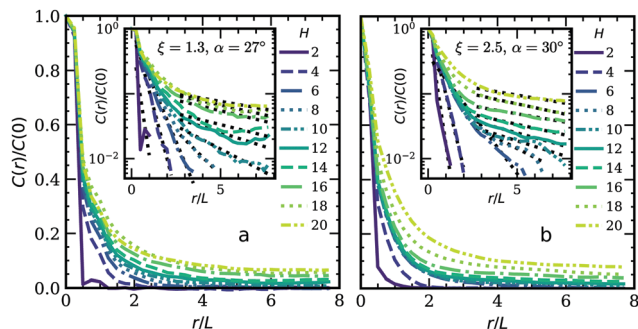
Fig. 7 $C(r)$ profiles for (a) $\xi = 1.3$, $\alpha = 27°$ and (b) $\xi = 2.5$, $\alpha = 30°$, normalized by $C(0)$. Each curve represents a different z, and the insets display the same data on a log scale. The black dotted lines are the linear fits for each correlation curve.

deviation, obtained for each particle aspect ratio ξ, marked by red points and error bars, respectively. For comparison, the linear fit of the data is shown by the dot-dashed line. For the sake of clarity, the specific shapes of the particles are also displayed in Fig. 6(a). The data show a good agreement with the linear fit, thereby indicating the goodness of the scaling $D/\dot{\gamma} \sim d_\perp^2$. It is worth mentioning, that similar analysis have been done using other particle characteristics sizes, specifically, the spherodiameter d and the equivalent spherical diameter. In both cases, the quality of the scaling analysis is reduced notably (data not shown).

Once the scaling using the characteristic length $d_\perp$ is confirmed, we propose $D \sim d_\perp^2 \dot{\gamma}$, as the most appropriate relationship between the particle diffusivity D and the local shear rate $\dot{\gamma}$. Fig. 5(b) illustrates the collapse of all the measured coefficients of diffusion D against $\dot{\gamma} d_\perp^2$. The line represents a linear regression, which is included for comparison. The data shows a reasonable correlation coefficient of $R = 0.94$. As the abscissa values increase, however, D values diverge from the linear trend. Despite the fact that we tried to introduce other scalings, involving the inverse of local solid fraction $\phi(z)$ ($d_\perp^2 \gamma / \phi(z)$) or $I(d_\perp^2 \gamma / \sqrt{I})$, none of them resulted in a better collapse of the data points.

Recently, P. Kharel and P. Rognon stated that the collective movement of partially jammed clusters of grains or granular vortices might enhance particle self-diffusion.[12] They found that the average vortex size is also a significant length to evaluate the D vs. $\dot{\gamma}$ scaling. Thus, in other to gain insight, we looked into the spatial vertical velocities correlations of the particles within each block located at a height z computing

$$C(r,z) = \langle v_z(r_i, z) v_z(r_j, z) \rangle = 1/N_c \sum_{i,j; \, j < i}^{N_c} v_z^i v_z^j \Xi(r - r_{ij}), \quad (3)$$

where r_i and r_j are the radial position of particles i and j, and $r_{ij} = r_j - r_i$ is the distance between particle i and j. The function $\Xi(x)$ yields 1 if $nL/4 < x < (n + 1) L/4$ else returns 0, and N_c is the number of pairs that fulfills the first condition. That is to say, the spatial correlation is averaged over all particle pairs located at the same distance, using a fine grid of width $L/4$.

Fig. 7 presents the profiles obtained from eqn (3) for (a) $\xi = 1.3$, $\alpha = 27°$ and (b) $\xi = 2.5$, $\alpha = 30°$, normalized by $C(0, z)$. The insets exhibit the same profiles on log–log scale, and the dotted black lines are linear fits of the tails. Note, the slope of the curve defines the inverse of the correlation length l_ξ, corresponding to each case. For locations closer to the bottom plate, our outcomes indicate that the particle velocities have shorter correlation length l_ξ, which is in the order of the particle dimension of L. However, it is also evidenced that l_ξ increases when exploring regions at higher locations, up to a point where H reaches the free surface. Thus, the system presents long-distance correlations close to the free surface, although the correlations can be classified as short-distance at regions, which are close to the bottom plane. The D values are less than the beforehand expected for short-distance correlations, while they are greater for long-distance. This observation suggests that a collective movement scale might also be involved in the D and $\dot{\gamma}$ dependency.

As the last point, it is worth mentioning that a similar analysis has been done, exploring the component of the diffusivity tensor in the y-direction and the off-diagonal components yz. The ESI† illustrates the outcomes obtained for the mean squared displacements (MSD) and the diffusivity in comparison with the shear rate fields. In those cases, we found that local diffusivity values do not correlate with the local shear rate values. Consequently, the simple scaling relation $D \sim d^2 \dot{\gamma}$ does not seem to be a good choice in those cases. Here, we could argue that the notably lower strength of the energy fluctuations might impact the quality of the numerical data. Thus, a more complete analysis is needed to confirm this. In addition, a natural progression of this work is to analyze other scaling laws, such as those based on granular temperature, like in ref. 14

4 Conclusions

In this study, we carried out DEM simulations of spherocylinders driven by gravity on an incline. Our aim was to quantify the diffusivity of non-spherical particles, assessing the scaling relations involving the particle dimensions and the shear rate $\dot{\gamma}$. Our efforts have identified that the particles follow a diffusive movement for temporal scales higher than one second. The diffusion coefficient D depends on the height, and as a consequence on the local non-linear shear rate. Our results indicate that D and $\dot{\gamma}$ correlate for almost all heights and aspect ratio ξ, excepting those values that are close to zones where $\dot{\gamma}$ varies non-linearly. Through finding the velocity PDFs and their skewness parameters, we have found that D values which do not collapse with $\dot{\gamma}$ coincide with skewness values far from zero. Thus, the PDFs are more asymmetric for the points where D and $\dot{\gamma}$ do not collapse. In addition, the spatial correlations of the velocity showed that the correlation length l_ξ is not constant, obtaining shorter values of l_ξ close to the bottom plane and higher values of l_ξ close to the free surface. Although our scaling analysis does not involve the particle correlation length

l_ξ, our finding suggests that collective movement may play a crucial role in diffusive dynamics of the present system.

One of the main findings emerging from this study is that $d_\perp(\xi)$ collapsed the scaling of D vs. $\dot\gamma$ for all aspect ratios ξ with reasonable accuracy. However, the scaling fails to reproduce this behavior for more elongated particles. Moreover, the efforts for introducing either solid fraction ϕ or inertial number I worsened the scaling. The question raised by this research is how to introduce the scale of the collective movement into the scaling. Further work needs to be done to establish a better scaling, especially for larger particles when submitted to variable $\dot\gamma$.

Conflicts of interest

There are no conflicts to declare.

Acknowledgements

Notes and references

1 S. S. Hsiau and M. L. Hunt, *Acta Mech.*, 1996, **114**, 121–137.
2 V. Garzó, *New J. Phys.*, 2011, **13**, 055020.
3 B. Utter and R. P. Behringer, *Phys. Rev. E*, 2004, **69**, 031308.
4 S. K. Hajra and D. V. Khakhar, *Phys. Fluids*, 2005, **17**, 013101.
5 S. B. Savage and R. Dai, *Mech. Mater.*, 1993, **16**, 225–238.
6 C. S. Campbell, *J. Fluid Mech.*, 1997, **348**, 85–101.
7 C. S. Campbell, *Powder Technol.*, 2006, **162**, 208–229.
8 N. Taberlet and P. Richard, *Phys. Rev. E: Stat., Nonlinear, Soft Matter Phys.*, 2006, **73**, 041301.
9 I. C. Christov and H. A. Stone, *Proc. Natl. Acad. Sci. U. S. A.*, 2012, **109**, 16012–16017.
10 I. C. Christov and H. A. Stone, *Granular Matter*, 2014, **16**, 509–515.
11 Y. Fan, P. B. Umbanhowar, J. M. Ottino and R. M. Lueptow, *Phys. Rev. Lett.*, 2015, **115**, 088001.
12 P. Kharel and P. Rognon, *Phys. Rev. Lett.*, 2017, **119**, 1–5.
13 P. Kharel and P. Rognon, *EPL*, 2018, **124**, 24002.
14 R. Artoni, M. Larcher, J. T. Jenkins and P. Richard, *Soft Matter*, 2021, **17**, 2596–2602.
15 P. Rognon and M. Macaulay, *Soft Matter*, 2021, **17**, 5271–5277.
16 S. S. Hsiau and M. L. Hunt, *J. Heat Transfer*, 1993, **115**, 541–548.
17 R. Cai, H. Xiao, J. Zheng and Y. Zhao, *Phys. Rev. E*, 2019, **99**, 1–12.
18 H. A. Makse and J. Kurchan, *Nature*, 2002, **415**, 614–617.
19 A. Tripathi and D. V. Khakhar, *J. Fluid Mech.*, 2013, **717**, 643–669.
20 Y. Fan, C. P. Schlick, P. B. Umbanhowar, J. M. Ottino and R. M. Lueptow, *J. Fluid Mech.*, 2014, **741**, 252–279.
21 Y. Zhao, H. Xiao, P. B. Umbanhowar and R. M. Lueptow, *AIChE J.*, 2018, **64**, 1550–1563.
22 P. B. Umbanhowar, R. M. Lueptow and J. M. Ottino, *Annu. Rev. Chem. Biomol. Eng.*, 2019, **10**, 129–153.
23 R. Cai, H. Xiao, I. C. Christov and Y. Zhao, *AIChE J.*, 2021, **67**, 1–17.
24 H. Ma and Y. Zhao, *Chem. Eng. Sci.*, 2017, **172**, 636–651.
25 R. C. Hidalgo, S. M. Rubio-Largo, F. Alonso-Marroquin and T. Weinhart, *EPJ Web Conf.*, 2017, **140**, 1–4.
26 R. C. Hidalgo, B. Szabó, K. Gillemot, T. Börzsönyi and T. Weinhart, *Phys. Rev. Fluids*, 2018, **7**, 074301.
27 T. Weinhart, A. R. Thornton, S. Luding and O. Bokhove, *Granul. Matter*, 2012, **14**, 531–552.
28 E. Hairer, C. Lubich and G. Wanner, *Acta Numerica*, 2003, **12**, 399–450.
29 Y. Wang, S. Abe, S. Latham and P. Mora, *Pure Appl. Geophys.*, 2006, **163**, 1769–1785.
30 T. Weinhart, R. Hartkamp, A. R. Thornton and S. Luding, *Phys. Fluids*, 2013, **25**, 070605.
31 M. Babic, *Int. J. Eng. Sci.*, 1997, **35**, 523–548.
32 I. Goldhirsch, *Granular Matter*, 2010, **12**, 239–252.
33 R. Artoni and P. Richard, *Phys. Rev. E*, 2015, **91**, 032202.
34 T. Weinhart, A. R. Thornton, S. Luding and O. Bokhove, *Granular Matter*, 2012, **14**, 531–552.